

# A highly accreting low-mass black hole hidden in the dust: *Suzaku* and *NuSTAR* observations of the NLS1 Mrk 1239

Jiachen Jiang<sup>1</sup>,<sup>\*</sup> Mislav Baloković,<sup>2,3</sup> Murray Brightman,<sup>4</sup> Honghui Liu<sup>5</sup>,<sup>\*</sup> Fiona A. Harrison<sup>4</sup> and George B. Lansbury<sup>6</sup>

<sup>1</sup>Department of Astronomy, Tsinghua University, Shuangqing Road, Beijing 100084, China

<sup>2</sup>Yale Center for Astronomy & Astrophysics, 52 Hillhouse Avenue, New Haven, CT 06511, USA

<sup>3</sup>Department of Physics, Yale University, P.O. Box 2018120, New Haven, CT 06520, USA

<sup>4</sup>Cahill Center for Astronomy and Astrophysics, California Institute of Technology, Pasadena, CA 91125, USA

<sup>5</sup>Department of Physics, Fudan University, 220 Handan Road, Shanghai 200433, China

<sup>6</sup>European Southern Observatory, Karl-Schwarzschild Street 2, D-85748 Garching bei München, Germany

Accepted 2021 May 4. Received 2021 April 26; in original form 2020 July 28

## ABSTRACT

We present torus modelling for the X-ray spectra of a nearby narrow-line Seyfert 1 galaxy Mrk 1239 ( $z = 0.0199$ ), based on archival *Suzaku*, *NuSTAR*, and *Swift* observations. Our model suggests very soft intrinsic power-law continuum emission of  $\Gamma \approx 2.57$  in 2019 and  $\Gamma \approx 2.98$  in 2007. By applying a correction factor to the unabsorbed X-ray luminosity, we find that Mrk 1239 is accreting near or around the Eddington limit. Our best-fitting spectral model also suggests a torus with a column density of  $\log(N_{\text{H,ave}}/\text{cm}^{-2}) = 25.0 \pm 0.2$  and a high covering factor of 0.90 in Mrk 1239, indicating that this source is most likely to be viewed almost face-on with  $i \approx 26^\circ$ . Our line of sight might cross the edge of the torus with  $N_{\text{H,los}} = 2\text{--}5 \times 10^{23} \text{ cm}^{-2}$ . The high Eddington ratio and the high line-of-sight column density makes Mrk 1239 one of the active galactic nuclei that are close to the limit where wind may form near the edge of the torus due to high radiation pressure.

**Key words:** black hole physics – galaxies: nuclei – galaxies: Seyfert – X-ray: galaxies.

## 1 INTRODUCTION

Mrk 1239 is a narrow-line Seyfert 1 galaxy (NLS1) that shows broad Balmer components of  $1000 \text{ km s}^{-1}$  and strong Fe [II] emission in the optical band (Osterbrock & Pogge 1985; Véron-Cetty, Véron & Gonçalves 2001). Ryan et al. (2007) estimated the mass of the supermassive black hole (BH) in the centre of Mrk 1239 to be  $7.8 \times 10^5 M_\odot$  by using the size of the broad-line region based on the  $\text{FWHM}(\text{H}\beta)\text{--}L_{\lambda 5100}$  relation (Kaspi et al. 2005) and  $1.3 \times 10^6 M_\odot$  on the basis of the  $\text{FWHM}(\text{H}\beta)\text{--}L_{\text{H}\beta}$  relation (Greene, Ho & Ulvestad 2006). By studying host bulge properties, Graham & Driver (2007) obtained a similar BH mass of  $5 \times 10^5\text{--}7 \times 10^6 M_\odot$ .

In addition to a low BH mass, Mrk 1239 also shows interesting properties across multiple wavelengths: in the radio band, relatively stronger radio emission than typical NLS1s along with evidence of a kiloparsec-scale radio jet was found (Doi et al. 2015), although Mrk 1239 is identified as a radio-quiet source (e.g. 50 mJy at 20 cm, Ulvestad, Antonucci & Goodrich 1995). These features were previously seen only in radio-loud NLS1s (e.g. Antón, Browne & Marchã 2008; Doi et al. 2012). In the near-infrared band, strong blackbody-like emission of  $T \approx 1200 \text{ K}$  peaking at  $2.2 \mu\text{m}$  was found (Rodríguez-Ardila & Mazzalay 2006). Such strong thermal emission might be related to the heated dusty torus located between the narrow-line region and the broad-line region of this system with a temperature

close to the sublimation limit (Riffel et al. 2006; Rodríguez-Ardila & Mazzalay 2006; Rodríguez-Ardila & Pastoriza 2006). In the optical band, polarization studies by Smith et al. (2004) suggest that the optical band of Mrk 1239 is dominated by polar-scattered emission. Our line of sight (LOS) towards the nuclei should pass through the upper layer of the torus.

In the X-ray band, Mrk 1239 shows particularly soft continuum emission. Rush et al. (1996) analysed the *ROSAT* spectrum of Mrk 1239 between 0.1 and 2.4 keV and found the soft X-ray spectrum was consistent with an absorbed power law with  $\Gamma = 2.94 \pm 0.04$ . A later study by Grupe, Mathur & Komossa (2004) suggested a similar conclusion of  $\Gamma \approx 3$  by analysing the *XMM-Newton* observation of this source in the 0.3–10 keV band. Such soft X-ray continuum emission indicates a high accretion rate in the central disc (e.g. Brightman et al. 2013). An Eddington ratio of  $\lambda_{\text{Edd}} \approx 2$  was obtained by modelling a multiwavelength SED of Mrk 1239 and assuming  $M_{\text{BH}} = 5 \times 10^6 M_\odot$  (Grupe et al. 2004).

Grupe et al. (2004) discovered an emission-line feature at 0.9 keV with an equivalent width of approximately 110 eV in the same *XMM-Newton* observation, which was interpreted as Ne IX emission line in their work. A supersolar Ne/O abundance might be required to explain this line feature.

Broad-band X-ray spectral analyses suggest that there are two light paths from Mrk 1239: one of the light paths is absorbed direct emission and the other is less absorbed (Grupe et al. 2004), which is consistent with the discovery of wavelength-dependent polarization degree in the optical emission of Mrk 1239 (Goodrich 1989).

\* E-mail: jcijiang@mail.tsinghua.edu.cn

In this work, we present a broad-band spectral model for the *Suzaku* and *NuSTAR* observations of Mrk 1239. In Section 2, we introduce our data reduction processes; in Section 3, we introduce a torus-based X-ray spectral model for Mrk 1239; in Section 4, we discuss and conclude our results.

## 2 DATA REDUCTION

### 2.1 *Suzaku*

*Suzaku* observed Mrk 1239 in 2007 for 63 ks (obs ID: 702031010). We produce cleaned event files for all operating XIS detectors (0, 1, 3) using AEPipeline v1.1.0 and the latest CALDB as of 2019 November. Source extraction regions are chosen to be circles with radii of 120 arcsec and background are taken from nearby regions with the same shape. We use tasks XISRMFGEN and XISSIMAR-FGEN to create response files for each detector. The spectra and response files of the front-illuminated instruments (XIS 0 and 3) spectra are combined by using the ADDSPEC tool. The combined spectrum is called FI spectrum hereafter. The spectrum of the back-illuminated instrument (XIS 1) is called BI spectrum hereafter. The spectra are grouped to have a minimum number of 20 counts per bin. During the spectral modelling, we ignore the energy band below 0.5 keV and the 1.7–2.5 keV band due to calibration uncertainty.

### 2.2 *NuSTAR*

Mrk 1239 was observed by the *NuSTAR* satellite in 2019 for  $\approx 21$  ks (observation ID 60360006002). The *NuSTAR* data are reduced using the standard pipeline NUPipeline v1.9.0 and instrumental responses from *NuSTAR* caldb V20200510. We extract the source spectra from circular regions with radii of 70 arcsec, and the background spectra from nearby circular regions of 110 arcsec on the same chip. The tool NUPRODUCTS is used for this purpose. The 3–40 keV band is considered for both FPMA and FPMB spectra. The energy band above 40 keV is dominated by background. The FPM spectra are grouped to have a minimum number of 20 counts per bin.

### 2.3 *Swift*

A *Swift* observation of Mrk 1239 with a length of 6 ks that was taken simultaneously with our *NuSTAR* observation is also considered (observation ID: 00081986001). The calibration file version used for XRT data reduction is 20190412. The standard pipeline XRTPRODUCTS v0.4.2 is used for data processing. The source spectrum is extracted from a circular region with a radius of 40 arcsec and the background spectrum is extracted from a circular region with a radius of 100 arcsec nearby. The spectrum is binned to have a minimum count of 20 per bin. We consider the 0.5–6 keV band of the XRT spectrum.

All the spectral analysis is processed by XSPEC v12.11.01 (Arnaud 1996) in HEASOFT v6.27.2.  $\chi^2$ -statistics is considered in this work. The Galactic column density towards Mrk 1239 is fixed at the nominal value  $4.16 \times 10^{20} \text{ cm}^{-2}$  (Willingale et al. 2013) if not specified.

## 3 SPECTRAL ANALYSIS

Fig. 1 shows the *Suzaku*, *Swift*, and *NuSTAR* spectra of Mrk 1239. A featureless, constant model is used to unfold the spectra only for demonstration purposes. The broad-band spectra of Mrk 1239 show similar obscuration as in other typical obscured Seyfert active galactic nuclei (AGNs, e.g. Baloković et al. 2018).

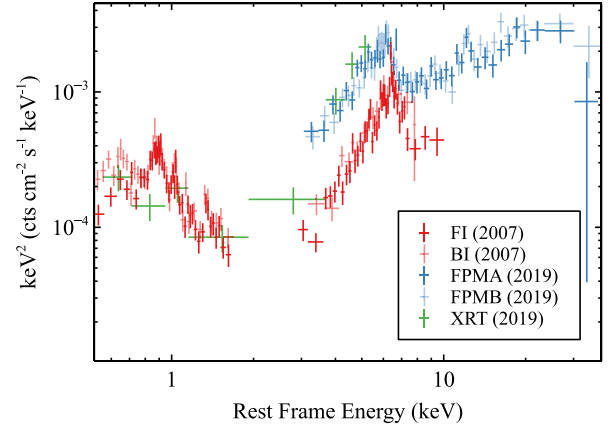


**Figure 1.** Unfolded *Suzaku*, *Swift*, and *NuSTAR* spectra of Mrk 1239. The response is unfolded using a featureless, constant model across the full band only for demonstration purposes. Blue: FPMA; faint blue: FPMB; red: FI; faint red: BI; green: XRT.

In the rest of this section, we first present an overlook of the spectral properties of Mrk 1239, and then we present a torus-based X-ray spectral model for the data.

### 3.1 Iron line and Compton hump

Previous studies suggest that the emission of Mrk 1239 consists of two parts, one direct absorbed emission and one less absorbed scattered emission (Goodrich 1989; Grupe et al. 2004). Therefore, we first model the *Suzaku* spectra of Mrk 1239 in the 2.5–10 keV band with an absorbed power-law model plus a scattered power-law model. The full model is  $\text{constant1} * \text{tbnew} * \text{zmshift} * (\text{vphabs} * \text{cabs} * \text{cutoffpl1} + \text{constant2} * \text{cutoffpl2})$ . The first constant1 is used to account for calibration uncertainty of different instruments. The second constant2 is the scaling factor ( $f_s$ ) of the scattered power-law component (cutoffpl2) relative to the direct obscured power-law component (cutoffpl1). The normalization parameters and the photon index ( $\Gamma$ ) of these two components are linked. The zmshift model is used to account for the source redshift ( $z = 0.0199$ ). The tbnew model accounts for Galactic absorption. The vphabs and cabs models are used to account for additional line-of-sight column density at the source's redshift.

Such a model can mostly describe the continuum emission in the hard X-ray band very well. A line-of-sight column density of  $5 \times 10^{23} \text{ cm}^{-2}$  is required. See the top panel of Fig. 2 for the corresponding data/model ratio plot. A narrow emission-line feature was found peaking at the rest frame 6.4 keV, which is the Fe K $\alpha$  emission from a cold emitter.

We apply the same model to the 3–10 keV band spectra of the *NuSTAR* observation. The data/model ratio plots are shown in the lower panel of Fig. 2. *NuSTAR* spectra also show narrow Fe K $\alpha$  emission and a strong Compton hump above 10 keV.

The existence of narrow Fe K $\alpha$  emission and Compton hump in the X-ray spectra suggest a cold, neutral emitter in this obscured system. Based on the evidence of an obscured continuum emission, we propose a torus interpretation (Antonucci 1993; Urry & Padovani 1995) for the X-ray reflector in Mrk 1239.

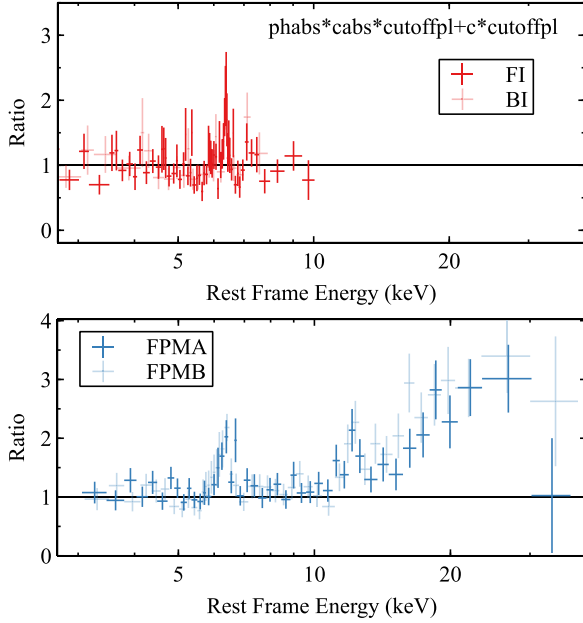


**Figure 2.** Data/model ratio plots using an absorbed power-law model plus a scattered power-law component. Both *Suzaku* and *NuSTAR* observations show a narrow emission-line feature at the rest frame 6.4 keV. FPM spectra also show a strong Compton hump feature above 10 keV.

### 3.2 Torus modelling

In this section, we model the full band spectra of Mrk 1239 using the *borus02* model introduced in Baloković et al. (2018).

The *borus02* model represents reprocessed X-ray radiation from an approximately toroidal geometry originally proposed by Brightman & Nandra (2011). It self-consistently accounts for the continuum and the fluorescent emission-line components. The main parameters relevant for the spectral shape of the reprocessed component in the *borus02* model are the torus covering factor, its average column density, inclination, and the relative abundance of iron. Despite the simplicity of the assumed geometry, these parameters form a complex and partially degenerate parameter space. The model is similar to, and broader than, the torus model of Brightman & Nandra (2011), which has been shown to be incorrect (Liu & Li 2015; Baloković et al. 2018). In this work, we make use of the table model ‘*borus02\_v200623sa.fits*’, which was calculated specifically to extend the photon index parameter space to accommodate sources with very steep intrinsic continua, such as Mrk 1239.

In Appendix A, we present a spectral model for Mrk 1239 using the *mytorus* model, an alternative model for torus emission (Murphy & Yaqoob 2009). The spectra of Mrk 1239 require a very soft power-law continuum, which is beyond the allowed parameter range of the public version of *mytorus*. So, we only present the analysis using the *borus02* model in this section.

The full model is `constant1 * tbnew * zshift * (borus02 + vphabs * cabs * cutoffpl1 + constant2 * cutoffpl2)` (MO0) in the XSPEC format.

During our spectral fitting process, the photon index ( $\Gamma$ ), the high-energy cut-off ( $E_{\text{cut}}$ ), and the normalization parameters of the *borus02* model are linked to the corresponding parameters of *cutoffpl1* and *cutoffpl2*. Previous optical polarization studies suggest our LOS might cross the upper layer of the torus in Mrk 1239 (e.g. Smith et al. 2004). We thus tie the half-opening

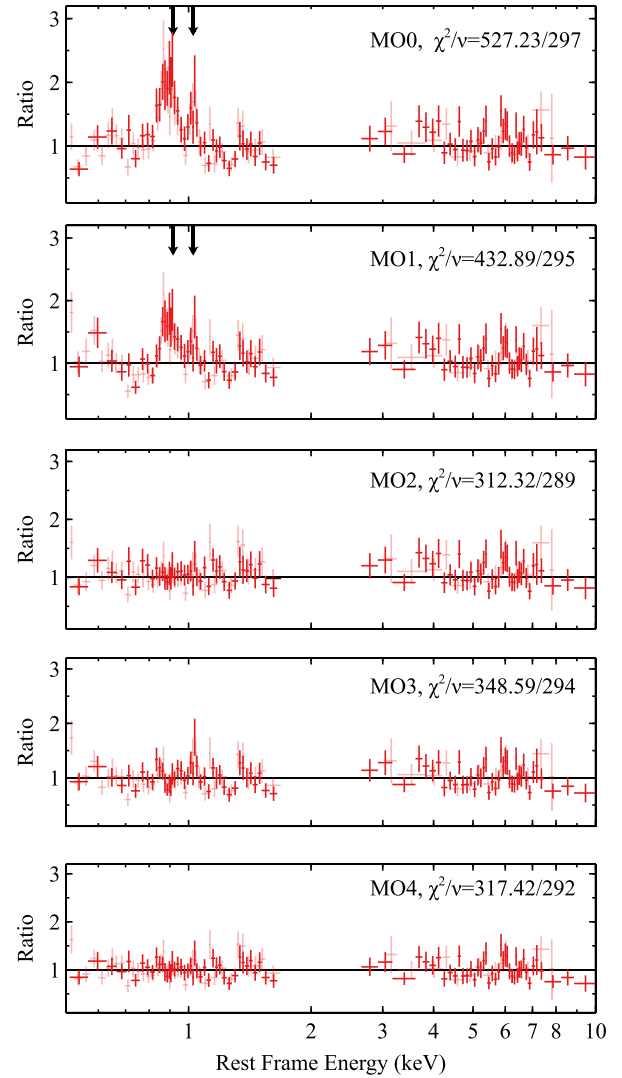


**Figure 3.** Data/model ratio plots of XIS spectra using model M0-M4. FI and BI spectra show significant evidence for an emission-line feature at 0.9 keV and tentative evidence for a second line at 1.0 keV (marked by black arrows). They correspond to Ne IX and Ne X lines, respectively.

angle and the inclination angle of the torus in our analysis. Similar approach was taken in the X-ray data analysis of other obscured AGNs (e.g. Kamraj et al. 2019). Later in Section 3.4.1, we will discuss the values of these two parameters in detail. The abundance parameters of *vphabs* model is linked to the iron abundance of *borus02* by using the solar abundances calculated from Anders & Grevesse (1989).

MO0 is able to provide a reasonable fit for the FI and BI spectra above 2.5 keV. But the fit is less satisfying in the soft X-ray band with  $\chi^2/\nu = 527.23/297$ . See the first panel of Fig. 3 for the corresponding data/model ratio plot.

### 3.3 Diffuse plasma emission in the soft X-ray band

#### 3.3.1 Ne x and Ne ix emissions

In order to fit the soft X-ray emission better, we include a diffuse hot plasma model *vmekal* (Liedahl, Osterheld & Goldstein 1995) by following the same approach for typical obscured Seyfert

**Table 1.** Best-fitting model parameters for the *Suzaku* observation of Mrk 1239. MO2 uses Gaussian line models to fit the narrow emission lines around 1 keV in the data; MO3 considers one vmekal component with supersolar Ne abundances; MO4 considers two vmekal components with the same supersolar Ne abundances. The other abundances of the vmekal models are assumed to be solar (Anders & Grevesse 1989).

Model	Parameter	Unit	MO2	MO3	MO4
tbnew	$N_{\text{H}}$	$10^{20} \text{ cm}^{-2}$	$3.9^{+0.4}_{-0.4}$	$4.1^{+0.3}_{-0.4}$	$3.8 \pm 0.6$
borus02	$\log(N_{\text{H,ave}})$	$\text{cm}^{-2}$	$25.0^{+0.4}_{-0.3}$	$25.3^{+0.2}_{-0.4}$	$25.0^{+0.4}_{-0.3}$
	Cfact	–	$0.91^{+0.03}_{-0.05}$	$0.92^{+0.03}_{-0.04}$	$0.92^{+0.02}_{-0.04}$
	$Z_{\text{Fe}}$	$Z_{\odot}$	$1.4^{+0.3}_{-0.2}$	$1.5 \pm 0.4$	$1.6^{+0.4}_{-0.3}$
vphabs	$N_{\text{H,los}}$	$10^{22} \text{ cm}^{-2}$	$55^{+6}_{-7}$	$47^{+6}_{-4}$	$48^{+4}_{-3}$
cutoffpl1,2	$\Gamma$	–	$2.98 \pm 0.02$	$2.98 \pm 0.02$	$2.98^{+0.02}_{-0.03}$
	$E_{\text{cut}}$	keV	500	500	500
	norm	$10^{-2}$	$2.2^{+0.4}_{-0.2}$	$1.9^{+0.4}_{-0.5}$	$1.6^{+0.4}_{-0.5}$
constant2	$f_{\text{s}}$	$10^{-3}$	$4.6 \pm 0.3$	$10.7 \pm 0.3$	$8.9 \pm 0.4$
vmekal1	kT	keV	$0.21^{+0.02}_{-0.03}$	$0.23^{+0.02}_{-0.03}$	$0.22^{+0.02}_{-0.03}$
	$Z_{\text{Ne}}$	$Z_{\odot}$	1	$4.7^{+2.3}_{-1.0}$	$4.9^{+1.2}_{-1.3}$
	norm	$10^{-4}$	$1.16^{+0.07}_{-0.10}$	$1.05^{+0.02}_{-0.04}$	$1.07 \pm 0.03$
vmekal2	kT	keV	–	–	$0.64^{+0.02}_{-0.03}$
	norm	$10^{-5}$	–	–	$2.2 \pm 0.2$
gauss1	Eline	keV	$0.884 \pm 0.007$	–	–
	$\sigma$	keV	$0.039^{+0.007}_{-0.010}$	–	–
	EW	eV	$117^{+23}_{-12}$	–	–
gauss2	Eline	keV	$1.024^{+0.010}_{-0.012}$	–	–
	$\sigma$	keV	$< 0.02$	–	–
	EW	eV	$56^{+14}_{-23}$	–	–
$\chi^2/\nu$			312.32/289	348.59/294	317.42/292

AGNs (e.g. Itoh et al. 2008; Hernández-García et al. 2017). In the beginning, we fix the abundances of vmekal at solar values (Anders & Grevesse 1989). The full model is constant1 \* tbnew \* zshift \* (borus02 + vmekal + vphabs \* cabs \* cutoffpl1 + constant2 \* cutoffpl2) (MO1). MO1 significantly improves our fit of the *Suzaku* spectra of Mrk 1239 in the soft X-ray band with  $\chi^2 = 432.89/298$ . See the second panel of Fig. 3.

However, two emission-line features are still seen around 1 keV. The first emission-line feature is at the rest frame 0.9 keV, which is similar to the Ne IX line identified in the *XMM-Newton* observation (Grupe et al. 2004). A second emission line is found around 1 keV. We first model these emission lines by using two simple Gaussian line models. The full model is constant1 \* tbnew \* zshift \* (gauss1 + gauss2 + borus02 + vmekal + vphabs \* cabs \* cutoffpl1 + constant2 \* cutoffpl2) (MO2).

By fitting the first line around 0.9 keV with gauss1, the fit is improved by  $\Delta\chi^2 = 104$  and three more free parameters. The best-fitting parameters are shown in Table 1. This line is at  $0.884 \pm 0.007$  keV, and lies at the energy of Ne IX emission. The equivalent width of the line is  $117^{+23}_{-12}$  eV. The best-fitting values are consistent with previous *XMM-Newton* measurements (Grupe et al. 2004).

By fitting the second line around 1 keV with gauss2, we are able to improve the fit by  $\Delta\chi^2 = 17$  and three more free parameters. The line is at  $1.024^{+0.010}_{-0.012}$  keV in the rest frame and the equivalent width is  $52^{+14}_{-23}$  eV. We only obtain an upper limit of its line width

( $\sigma < 0.02$  keV). This narrower emission line at 1.03 keV can be interpreted as Ne X emission line. A quick F-test based on the  $\chi^2$  improvement suggests an F statistic value of 7.7, which is much less significant than the Ne IX line. We conclude that we find tentative evidence for Ne X emission line in addition to strong evidence of Ne IX line as in previous analyses.

### 3.3.2 Hot diffuse plasma with supersolar Ne abundances

The two narrow emission lines lie well with the energy of Ne X and Ne IX lines. As Grupe et al. (2004) argued, super Ne abundances relative to oxygen might be needed to explain these lines. Instead of modelling the lines with simple gauss models, we propose a physical model with a supersolar Ne abundance for the data. To do so, the Ne abundance parameter ( $Z_{\text{Ne}}$ ) of the vmekal component is allowed to be free during spectral fitting (MO3). Other abundances are fixed at solar (Anders & Grevesse 1989).

MO3 is able to provide a better fit than MO1 with  $\Delta\chi^2 = 84.3$  and one more parameter. Corresponding data/model ratio plots are shown in the fourth panel of Fig. 3. Best-fitting parameters are shown in Table 1. MO3 offers a reasonable fit to the emission line at 0.88 keV with a supersolar Ne abundance, although some residuals still remain around 0.86 keV. The second emission line at 1.02 keV cannot be modelled by MO3. Therefore, we add a second vmekal component (MO4). The Ne abundances of these two vmekal components are linked. MO4 provides a very good fit of the data with  $\chi^2/\nu = 317.42/292$ . The best-fitting parameters are shown in Table 1, and



**Table 2.** Best-fitting model parameters for two epochs. *l* means this parameter is linked during our spectral fitting.

Model	Parameter	Unit	Su	Nu&Sw
tbnew	$N_{\text{H}}$	$10^{20} \text{ cm}^{-2}$	$3.8 \pm 0.4$	<i>l</i>
borus02	$\log(N_{\text{H,ave}})$	$\text{cm}^{-2}$	$25.0 \pm 0.2$	<i>l</i>
	Cfact	–	$0.90^{+0.04}_{-0.03}$	<i>l</i>
	$Z_{\text{Fe}}$	$Z_{\odot}$	$1.3^{+0.4}_{-0.3}$	<i>l</i>
vphabs	$N_{\text{H,los}}$	$10^{22} \text{ cm}^{-2}$	$52^{+7}_{-6}$	$20^{+4}_{-3}$
cutoffpl1,2	$\Gamma$	–	$2.98 \pm 0.02$	$2.57^{+0.03}_{-0.02}$
	$E_{\text{cut}}$	keV	$>480$	<i>l</i>
	norm	$10^{-2}$	$1.4 \pm 0.4$	$0.6 \pm 0.3$
constant2	$f_{\text{S}}$	$10^{-3}$	$8.3 \pm 0.2$	$7.4 \pm 0.3$
vmekal1	kT	keV	$0.21 \pm 0.02$	<i>l</i>
	$Z_{\text{Ne}}$	$Z_{\odot}$	$4.9^{+1.3}_{-1.0}$	<i>l</i>
	norm	$10^{-4}$	$1.10 \pm 0.04$	<i>l</i>
vmekal2	kT	keV	$0.63 \pm 0.02$	<i>l</i>
	norm	$10^{-5}$	$3.0 \pm 0.2$	<i>l</i>
	$\chi^2/\nu$		519.97/468	

corresponding data/model ratio plots are shown in the last panel of Fig. 3.

In comparison with MO2 where gauss models are used, the fit using MO4 has a slightly higher  $\chi^2$  ( $\Delta\chi^2 = 5.1$ ) but three fewer parameters. In the end, we decide to choose MO4 as our best-fitting model instead of MO2. Because MO4 provides a more physical interpretation to the narrow emission lines.

In conclusion, two diffuse plasma components are required to fit the soft X-ray spectrum of Mrk 1239: one has a temperature of  $kT \approx 0.22$  keV and the other one has a temperature of  $kT \approx 0.64$  keV. A supersolar Ne abundance of  $Z_{\text{Ne}} = 4.9^{+1.2}_{-1.3} Z_{\odot}$  is needed. Buhariwalla et al. (2020) suggested that these hot plasma components may be associated with the star-burst region in the host galaxy of Mrk 1239. This component has been often found in the soft X-ray emission of many obscured sources (e.g. Franceschini et al. 2003). When the AGN emission is high and not heavily obscured, this component still exists, but overwhelmed by the central AGN emission.

### 3.4 Multi-epoch spectral analysis

In this section, we apply MO4 to all the spectra of Mrk 1239 simultaneously. As shown in Fig. 1, the soft X-ray band of Mrk 1239, which is dominated by distant diffuse plasma emission, shows a consistent flux level in two epochs. The signal-to-noise (S/N) of *Swift* XRT data does not allow us to investigate the soft X-ray emission during the second epoch in detail. Therefore, we link the parameters of diffuse plasma emission components for two epochs. Other parameters, such as the torus inclination angle, the average column density, and the iron abundance of the torus, are expected to be consistent on observable time-scales. They are thus linked during our spectral fitting too.

MO4 provides a good fit to the data of both epochs. The best-fitting parameters are shown in Table 2, and the best-fitting data/model ratio plots are shown in Fig. 4.

#### 3.4.1 The inclination angle and the opening angle of the torus

The best-fitting average column density of the torus  $\log(N_{\text{H,ave}})$  is approximately  $10^{25} \text{ cm}^{-2}$ . The line-of-sight column density  $N_{\text{H,los}}$  is

$2\text{--}5 \times 10^{23} \text{ cm}^{-2}$ , which is 2 orders of magnitudes lower than  $N_{\text{H,ave}}$ . In MO4, the inclination angle ( $i$ ) and the half-opening angle<sup>1</sup> of the torus (Cfact) are linked in our analysis as in Kamraj et al. (2019) – our LOS might cross the edge of the torus where the column density is only 2–5 per cent of the average column density of the whole torus.

In this part of the section, we investigate how valid the  $\text{Cfact} \approx \cos(i)$  relation is by allowing these two parameters to be free in our analysis. All the spectra are used for this test. Fig. 5 shows the  $\chi^2$  distribution on the Cfact and  $i$  parameter plane. The XSPEC tool STEPPAR is used to do so. Only lower limit has been obtained: a  $3\sigma$  uncertainty range of Cfact is  $>0.815$  and that of  $\cos(i)$  is  $>0.6$ . They suggest a half-opening angle smaller than  $35^\circ$  and an inclination angle smaller than  $53^\circ$ . The model is more sensitive to Cfact/the half-opening angle of the torus, because this parameter directly modifies the continuum emission. The constraint of  $i$  is relatively weaker as the model is less sensitive to this parameter.

We show the  $\text{Cfact} = \cos(i)$  reference line in Fig. 5. Our assumption of  $\text{Cfact} = \cos(i)$  lines well within the  $1\sigma$  uncertainty range, indicating that these two parameters approach a similar value in our analysis. In this case, our LOS might cross the edge of a torus which has a small half-opening angle. Similar conclusions were found in the optical polarization studies: Mrk 1239 turns out to be a polar-scattered NLS1 in which our LOS passes the upper layer of its torus (Smith et al. 2004).

By linking these two parameters, we obtain a better constraint of both parameters  $\text{Cfact} = \cos(i) = 0.90^{+0.04}_{-0.03}$  (90 per cent confidence range) as shown in Table 2. This best-fitting value corresponds to a small half-opening and inclination angle of approximately  $26^\circ$ .

A covering factor that is as high as  $\approx 90$  per cent in Mrk 1239 has been also seen in *NuSTAR* observations of other obscured Sy1 galaxies but with lower accretion rates than in Mrk 1239 (e.g. Baloković et al. 2018; Kamraj et al. 2019).

#### 3.4.2 Ultra-soft X-ray continuum emission

The photon index of the power-law continuum emission is  $2.98 \pm 0.02$  for the *Suzaku* epoch and  $2.57^{+0.03}_{-0.02}$  for the *NuSTAR* and *Swift* epoch. Despite the obscured nature, the very soft X-ray continuum emission from the hot corona of Mrk 1239 is very similar to that of other NLS1s (e.g. Gallo 2018).

In particular, X-ray studies of a sample of unobscured, extreme ultra-soft NLS1s suggest similar continuum emission with  $\Gamma > 2.5$  (Jiang et al. 2020). Detailed modelling of their multiwavelength SEDs suggest an Eddington ratio that is around or a few times higher than the Eddington limit (e.g. Jin et al. 2009; Jiang et al. 2020). Strong soft excess emission is shown in their data, and can be interpreted as part of reflection from a highly ionized inner disc region as well broad Fe K emissions (Jiang et al. 2020). Unfortunately, due to the obscuration along our LOS towards Mrk 1239, we are unable to constrain the soft excess emission from the centre of the AGN in Mrk 1239.

In Section B, instead of investigating in the soft X-ray band, we discuss possible contribution of a disc reflection component in the hard X-ray band, particularly in the observed back-scattering Compton hump.

<sup>1</sup>The covering factor of a toroid-shaped torus is approximately the cosine of its half-opening angle.

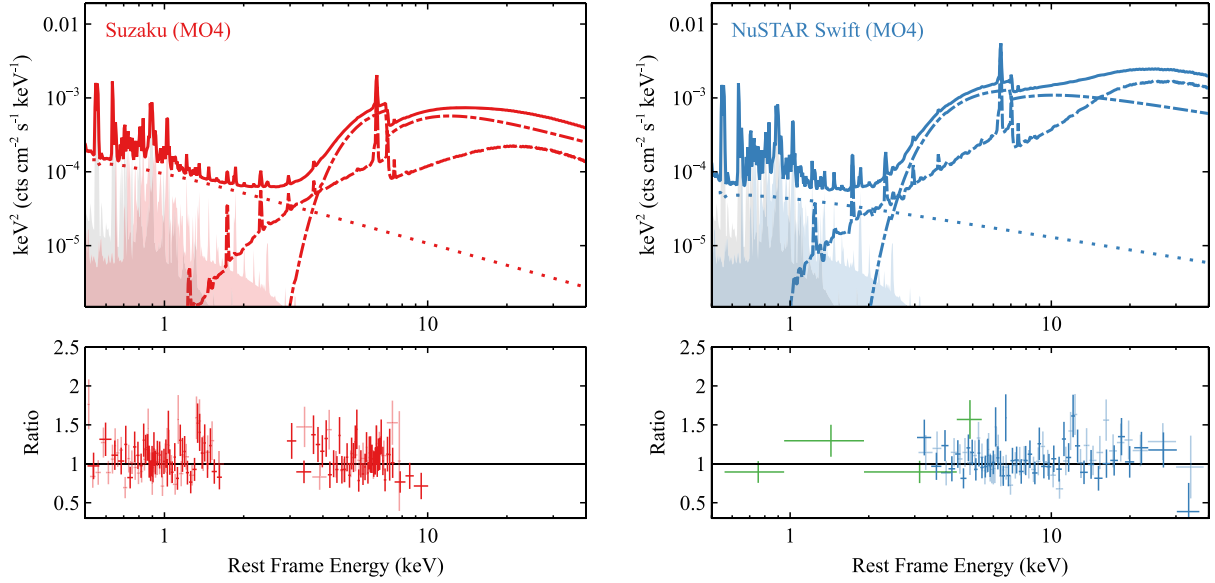


**Figure 4.** Top: best-fitting models for the *Suzaku* (left), *NuSTAR*, and *Swift* (right) spectra of Mrk 1239 using MO4. Thick lines: total model; shaded regions: two diffuse hot plasma emission components; dashed lines: torus model; dash-dotted lines: absorbed power-law continuum emission; dotted lines: scattered power-law components. Bottom: corresponding data/model ratio plots.

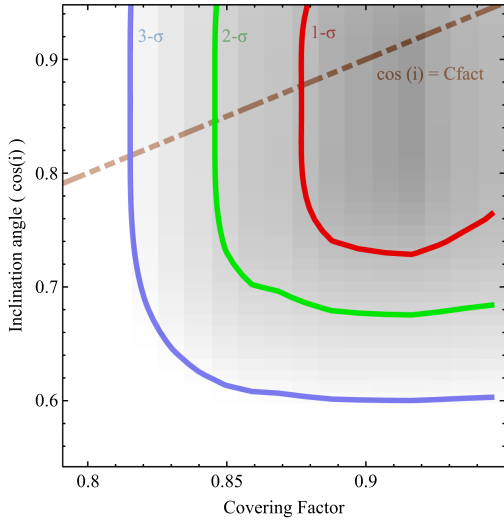


**Figure 5.**  $\chi^2$  distribution on the Cfact and  $i$  parameter plane. The red, green, and blue solid lines show the  $1\sigma$ ,  $2\sigma$ , and  $3\sigma$  uncertainty ranges. The dash-dotted line shows the  $C_{\text{fact}} = \cos(i)$  line.

## 4 DISCUSSION

### 4.1 The accretion rate of Mrk 1239

Our best-fitting model suggests a very soft intrinsic power-law emission of  $\Gamma = 2.6$ – $3$ . The softness of the continuum emission suggests a high mass accretion rate in the disc (e.g. Brightman et al. 2013, and references therein).

We estimate the Eddington ratio of Mrk 1239 by using its 2–10 keV luminosity. The absorption-corrected flux of Mrk 1239 is  $1.0 \times 10^{-11} \text{ erg cm}^{-2} \text{ s}^{-1}$  in 2007 and  $8.0 \times 10^{-12} \text{ erg cm}^{-2} \text{ s}^{-1}$  in 2019 calculated by our best-fitting model. Assuming a BH mass of  $1 \times 10^6 M_{\odot}$ , they correspond to  $L_X = 7.1$ – $8.8 \times 10^{42} \text{ erg s}^{-1} = 0.06$ – $0.07 L_{\text{Edd}}$ . When considering a typical correction factor of  $\kappa =$

10–20 for this luminosity (Vasudevan & Fabian 2007), we estimate Mrk 1239 has a bolometric luminosity of 0.6–1.4 of the Eddington limit assuming a BH mass of  $10^6 M_{\odot}$ .

Previous independent measurements of the mass of the SMBH in Mrk 1239 all agree with a relatively low value of  $\approx 1 \times 10^6 M_{\odot}$  (see Section 1). We consider the largest measurement uncertainty in the literature: Graham & Driver (2007) estimated  $M_{\text{BH}} = 5 \times 10^5$ – $7 \times 10^6 M_{\odot}$  by using the host bulge properties in Mrk 1239. After taking into account the uncertainty of BH mass measurements, our estimation of  $\lambda_{\text{Edd}}$  is 0.1–2.8 for Mrk 1239.

Similar conclusions were found in Grupe et al. (2004) where a multiwavelength SED was used for the calculation of the Eddington ratio:  $\lambda_{\text{Edd}} \approx 2$  assuming  $M_{\text{BH}} = 5 \times 10^6 M_{\odot}$ . Buhariwalla et al. (2020) found an Eddington ratio of  $\lambda_{\text{Edd}} = 1$ – $1.5$ . Yao et al. (2018) applied a correction factor to the  $L_{\lambda 5100}$  of Mrk 1239 and obtained  $\lambda_{\text{Edd}} = 1.12$ . The uncertainties of their estimations were not mentioned in their work. But they are all consistent with our measurement.

In conclusion, Mrk 1239 is one of the most extreme AGNs that are accreting near or around the Eddington limit.

### 4.2 Stability of the dusty torus in Mrk 1239

The high accretion rate in the central engine of Mrk 1239 may explain the high-temperature blackbody emission in the near-infrared band (Rodríguez-Ardila & Mazzalay 2006). The dusty torus is heated by the radiation from the inner accretion region close to the sublimation limit. In this section, we discuss the stability of such a heavy torus and the radiation pressure from the luminous nucleus on to the torus.

Laor & Draine (1993), Scoville & Norman (1995), and ay, Quataert & Thompson (2005) calculate the effective Eddington ratio for cool dusty gas, which is found to be much lower than the Eddington ratio for ionized dust-free gas. As an example, the black solid line in Fig. 6 shows the effective Eddington limit for different column densities. The line is adopted from Fabian et al. (2009). The radiation pressure will play an important role for systems that correspond to the right

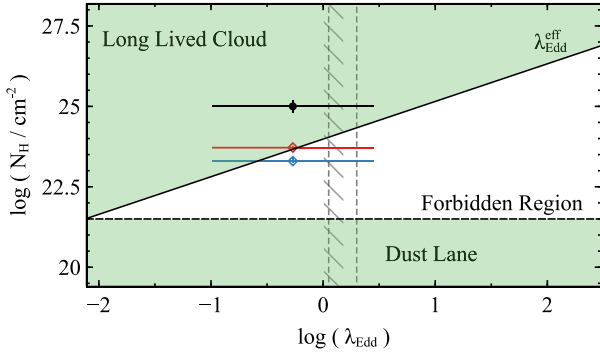


**Figure 6.** Eddington ratio  $\lambda_{\text{Edd}}$  versus column density diagram. The solid black line shows the effective Eddington limit for different values of column density. The dashed line shows the typical column density of the dust lanes in host galaxies. Obscuring dusty materials will be blown away due to radiation pressure when luminosity exceeds the effective Eddington limit (white forbidden region in the figure). Most *Swift* BAT AGNs lie within the green shaded region (Fabian et al. 2009; Ricci et al. 2017b). Some exceptional dusty quasars at higher redshifts, e.g.  $z > 0.2$ , are found to be located in the forbidden region (Lansbury et al. 2020). The black circle shows the column density of the torus in Mrk 1239. The red and blue diamonds show the line-of-sight column density in 2007 and 2019, respectively. The luminosity of the nuclei in Mrk 1239 may exceed the effective Eddington limit in the upper layer of the torus. Wind might be forming on the edge due to high radiation pressure. The left and right grey dashed lines show the values  $\lambda_{\text{Edd}}$  given in Yao et al. (2018) and Grupe et al. (2004), respectively. The shaded region shows the range of  $\lambda_{\text{Edd}}$  estimated by Buhariwalla et al. (2020).

of the solid line. The obscuring dusty materials will be blown away due to high radiation pressure when luminosity exceeds the effective Eddington limit. The dashed line shows the typical column density of galactic dust lane that may make contribution to the X-ray spectrum.

Large X-ray surveys, e.g. the *Swift* BAT catalogue, indeed find that most of the known AGNs tend to avoid the forbidden region of this diagram (Fabian et al. 2009; Ricci et al. 2017b) and lie within the green shaded region in Fig. 6. Some exceptional cases are, however, found in very luminous dusty quasars at higher redshifts (e.g.  $z > 0.2$ , Lansbury et al. 2020).

We show Mrk 1239 in the  $N_{\text{H}}-\lambda_{\text{Edd}}$  diagram in Fig. 6, and it is located on the edge of the ‘long-lived cloud’ region. The line-of-sight column density of Mrk 1239 is estimated to be  $2\text{--}5 \times 10^{23} \text{ cm}^{-2}$ . The luminosity of Mrk 1239 can exceed the effective Eddington limit at this low value of column density. Therefore, radiation-pressure-driven wind might be forming near the edge of the torus along our LOS.

Last but not least, it is important to note that the  $\text{H}\alpha$  emission of Mrk 1239 shows an asymmetric profile with a minimum polarization degree in the blue wing and a maximum degree in the red wing, which might be related to a radial outflow (Smith et al. 2004).

Future high-S/N, TES-based (Transition Edge Sensor) observations, such as from *XRISM* with a spectral resolution of 2.5 eV, might enable us to look for any evidence of wind absorption features in the X-ray spectra, such as blueshifted Fe K edges.

### 4.3 The variability of the line-of-sight column density of Mrk 1239

In Section 3.4.1, we estimate the half-opening angle and the inclination angle of the torus in Mrk 1239 by allowing them to vary during spectral fitting. The results suggest an inclination angle smaller than  $53^\circ$  and a half-opening angle smaller than  $35^\circ$ . When we link

these two parameters during spectral fitting, the best-fitting value corresponds to a small half-opening angle of approximately  $26^\circ$ .

In this scenario, our LOS crosses the upper edge of the torus in Mrk 1239. Therefore, measured  $N_{\text{H,los}}$  corresponds to the column density near the edge of the torus, which is only a few per cent of the average column density of the torus:  $N_{\text{H,los}} = 5.2^{+0.7}_{-0.6} \times 10^{23} \text{ cm}^{-2}$  in 2007 and  $2.0^{+0.4}_{-0.3} \times 10^{23} \text{ cm}^{-2}$  in 2019. A similar  $N_{\text{H,los}}$  was found in the *XMM-Newton* observation of Mrk 1239 in 2001 ( $N_{\text{H,los}} \approx 3 \times 10^{23} \text{ cm}^{-2}$ , Grupe et al. 2004). These observations were separated by 18 yr and suggest that some variability of  $N_{\text{H,los}}$  with a small amplitude may exist in Mrk 1239 during this period.

As shown in the previous section, radiation-pressure-driven dusty wind may be forming near the edge of the torus when  $N_{\text{H}} < 10^{24} \text{ cm}^{-2}$ . If true, our LOS intercepts with the wind and some variability of  $N_{\text{H,los}}$  is expected. In comparison, the average column density of the torus is as high as  $10^{25} \text{ cm}^{-2}$ . The radiation pressure from the central region of the AGN in Mrk 1239 is not high enough to ‘blow’ wind from the equatorial plane of torus.

Alternatively, a clumpy torus model may also explain the variability in  $N_{\text{H,los}}$ . In the unification paradigm of AGNs (Antonucci 1993), Seyfert 1 AGNs (Sy1s) and Seyfert 2 AGNs (Sy2s) are distinguished by their inclination angles, i.e. whether our LOS crosses the torus. This standard picture assumes a homogeneous dusty torus. However, observations suggest that the LOS obscuration is determined not only by inclination angle but also by the probability of absorption clouds intercepting our LOS (Nenkova et al. 2008). Evidence for the clumpiness of the torus includes a large and rapid variability of the absorber observed in several sources (e.g. Risaliti, Elvis & Nicastro 2002; Bianchi, Maiolino & Risaliti 2012; Laha et al. 2020). Markowitz, Krumpe & Nikutta (2014) estimated the probability of an absorption event regardless of constant absorption due to non-clumpy material to be 0.003–0.16 for Sy1s. Dramatic changes of  $N_{\text{H,los}}$  up to a few orders of magnitude have indeed been seen in Sy1s on observable time-scales (e.g. Simm et al. 2018).

Unfortunately, archival observations are not sufficient enough to distinguish these two models for the small variability of  $N_{\text{H,los}}$  in Mrk 1239. As concluded in the previous section, a search for absorption features, e.g. blueshifted absorption edge due to dusty wind, is required when TES-based observations are available.

## 4.4 Mrk 1239 as a polar-scattered Sy1

### 4.4.1 The opening angle of the torus in Mrk 1239

As introduced above, Sy1s and Sy2s are intrinsically the same type of object but viewed from different inclination angles in the unification paradigm of AGNs (Antonucci 1993), which is supported by the detection of polarized broad lines in Sy2s (e.g. Antonucci & Miller 1985; Miller & Goodrich 1990; Young et al. 1996). Meanwhile, it is believed that two scattering regions, the equatorial plane (e.g. Goodrich & Miller 1994; Cohen et al. 1999; Cohen & Martel 2002) and the ionization cone on the torus axis (e.g. Antonucci 1983; Smith et al. 2002), both contribute to the polarized emission in AGNs.

Smith et al. (2004) argued that the inclination angle plays an important role in the interpretation of the detected polarization in AGNs. Polar-scattered Sy1s represent a bridge between Sy1s and Sy2s. Their optical polarization position angle is perpendicular to the projected radio source axis as in Sy2s (Smith et al. 2004), while the majority of Sy1s show optical polarization properties that are not consistent with polar scattering (e.g. Antonucci 1983; Smith et al. 2002). This is because our LOS may intercept with the edge of the torus in polar-scattered Sy1s, e.g. Mrk 1239 (Smith et al. 2004),

where the equatorial emission is obscured by the dusty torus and makes little contribution to the detected optical polarization.

Our torus modelling of the X-ray spectra of Mrk 1239 provides another supporting evidence for this model. Our results suggest that the data are consistent with the case that our LOS intercepts with the upper edge of the torus.

Assuming a toroid-shaped inhomogeneous torus, we obtain an upper limit of  $35^\circ$  for the half-opening angle parameter at  $3\sigma$  uncertainty level (see Section 3.4.1). Such a low half-opening angle corresponds to a very high covering factor for Mrk 1239, e.g.  $C_{\text{fact}} > 0.81$ .

A similar covering factor was found in Mrk 231, another polar-scattered Sy1. For instance, Piconcelli et al. (2013) found that Mrk 231 shows two partial-covering absorbers with  $N_{\text{H}} \approx 10^{22}$  and  $10^{24} \text{ cm}^{-2}$ . A very high covering factor of more than 0.9 and 0.8 are, respectively, found for these two absorbers (Piconcelli et al. 2013). Interestingly, Smith et al. (2004) found that the optical polarization spectra of Mrk 1239 and Mrk 231 are very similar too: their continuum polarization rises at shorter wavelengths and peaks at the red wing of their broad lines.

#### 4.4.2 Comparison with other polar-scattered Sy1s

Polar-scattered Sy1s, including Mrk 1239, often show significant absorption features in the X-ray band, which is in agreement with the picture that our LOS passes close to their torus opening angles (e.g. Jiménez-Bailón et al. 2008; Laha, Dewangan & Kembhavi 2011; Piconcelli et al. 2013; Newman et al. 2021). For instance, the polar-scattered Sy1 Mrk 704 shows not only a partial covering neutral absorber with  $N_{\text{H}} \approx 10^{23} \text{ cm}^{-2}$  and  $C_{\text{fact}} = 0.22$  but also two layers of warm absorbers that are associated with the broad-line region (Laha et al. 2011).

Meanwhile, polar-scattered Sy1s show a variety of X-ray spectral features. For example, the neutral absorber in Mrk 704 has a much lower covering factor than those in Mrk 1239 and Mrk 231. This indicates that the torus opening angles in polar-scattered Sy1s may not be uniform. Ricci et al. (2017a) applied a torus model to a sample of *Swift* BAT AGNs. For the 12 objects with constrained torus half-opening angles, they found a median value of  $58 \pm 3^\circ$ . Mrk 1239 and Mrk 704 are, respectively, located in the lower and higher ends of the global distribution of torus opening angles.

Besides, as demonstrated in this work and Piconcelli et al. (2013), Mrk 231 and Mrk 1239 show no significant evidence of reprocessing emission from the innermost region, e.g. disc reflection (see Section B). In comparison, other polar-scattered Sy1s show evidence of either broad Fe K $\alpha$  emission (e.g. Fairall 51, Svoboda et al. 2015) or soft excess emission from the innermost accretion region (e.g. NGC 3227 and Mrk 704, Laha et al. 2011; Newman et al. 2021).

## 5 CONCLUSIONS

We present a torus model for the X-ray spectra of the NLS1 Mrk 1239 based on archival *Suzaku*, *NuSTAR*, and *Swift* observations. The main results are as follows.

(i) The primary X-ray continuum of Mrk 1239 is described by a power law with slope  $\Gamma = 2.6\text{--}3.0$ . Such a soft continuum suggests that Mrk 1239 is one of the most extreme AGNs that are accreting near or around the Eddington limit. By applying a correction factor to its X-ray luminosity, we obtain  $\lambda_{\text{Edd}} = 0.1\text{--}2.8$  after taking into account the uncertainty of the BH mass measurements.

(ii) At such a high accretion rate, the radiation pressure from the central region of the AGN may drive wind near the edge of the torus where column density is around  $10^{23} \text{ cm}^{-2}$ . Future high-S/N, TES-based X-ray observations may reveal more spectral details of Mrk 1239, e.g. blueshifted absorption edge features.

(iii) The X-ray data of Mrk 1239 are consistent with the optical polarization model for polar-scattered Sy1s where our LOS intercepts with the upper edge of the torus. The LOS column density of Mrk 1239 is only a few per cent of the average column density of the torus in this source. The half-opening angle of the torus is estimated to be around  $26^\circ$ , corresponding to a very high covering factor of 90 per cent. Such a small opening angle makes Mrk 1239 near the lower end of the global torus opening angle distribution of AGNs.

## ACKNOWLEDGEMENTS

This paper was written during the worldwide COVID-19 pandemic in 2020–2021. We acknowledge the hard work of all the health care workers around the world. We could not have finished this paper without their protection. JJ acknowledges support from the Tsinghua Shui’Mu Scholar Program and the Tsinghua Astrophysics Outstanding Fellowship. MB acknowledges support from the YCAA Prize Postdoctoral Fellowship. This work made use of data from the *NuSTAR* mission, a project led by the California Institute of Technology, managed by the Jet Propulsion Laboratory, and funded by NASA, and data obtained from the *Suzaku* satellite, a collaborative mission between the space agencies of Japan (JAXA) and the USA (NASA). This research has made use of the *NuSTAR* Data Analysis Software (NuSTARDAS) jointly developed by the ASI Science Data Center and the California Institute of Technology.

## DATA AVAILABILITY

All the data can be downloaded from the HEASARC website at <https://heasarc.gsfc.nasa.gov>.

## REFERENCES

- Anders E., Grevesse N., 1989, *Geochim. Cosmochim. Acta*, 53, 197
- Antón S., Browne I. W. A., Marchã M. J., 2008, *A&A*, 490, 583
- Antonucci R. R. J., 1983, *Nature*, 303, 158
- Antonucci R., 1993, *ARA&A*, 31, 473
- Antonucci R. R. J., Miller J. S., 1985, *ApJ*, 297, 621
- Arnaud K. A., 1996, in George H. J., Jeannette B., eds, *XSPEC: The First Ten Years*, Vol. 101, *Astronomical Data Analysis Software and Systems V*, p. 17
- Baloković M. et al., 2018, *ApJ*, 854, 42
- Bianchi S., Maiolino R., Risaliti G., 2012, *Adv. Astron.*, 2012, 782030
- Brightman M. et al., 2013, *MNRAS*, 433, 2485
- Brightman M., Nandra K., 2011, *MNRAS*, 413, 1206
- Buhariwalla M. Z., Waddell S. G. H., Gallo L. C., Grupe D., Komossa S., 2020, *ApJ*, 901, 118
- Cohen M. H., Martel A. R., 2002, in Crenshaw D. M., Kraemer S. B., George I. M., eds, *ASP Conf. Ser. Vol. 255, Mass Outflow in Active Galactic Nuclei: New Perspectives*. Astron. Soc. Pac., San Francisco, p. 255
- Cohen M. H., Ogle P. M., Tran H. D., Goodrich R. W., Miller J. S., 1999, *AJ*, 118, 1963
- Dauser T., García J., Walton D. J., Eikmann W., Kallman T., McClintock J., Wilms J., 2016, *A&A*, 590, A76
- Doi A., Nagira H., Kawakatu N., Kino M., Nagai H., Asada K., 2012, *ApJ*, 760, 41
- Doi A., Wajima K., Hagiwara Y., Inoue M., 2015, *ApJ*, 798, L30
- Fabian A. C., Vasudevan R. V., Mushotzky R. F., Winter L. M., Reynolds C. S., 2009, *MNRAS*, 394, L89



Franceschini A. et al., 2003, *MNRAS*, 343, 1181

Gallo L., 2018, Proc. Sci., Revisiting Narrow-Line Seyfert 1 Galaxies and their Place in the Universe. SISSA, Trieste, PoS#34

García J., Dauser T., Reynolds C. S., Kallman T. R., McClintock J. E., Wilms J., Eikmann W., 2013, *ApJ*, 768, 146

Goodrich R. W., 1989, *ApJ*, 342, 224

Goodrich R. W., Miller J. S., 1994, *ApJ*, 434, 82

Graham A. W., Driver S. P., 2007, *ApJ*, 655, 77

Greene J. E., Ho L. C., Ulvestad J. S., 2006, *ApJ*, 636, 56

Grupe D., Mathur S., Komossa S., 2004, *AJ*, 127, 3161

Guainazzi M. et al., 2016, *MNRAS*, 460, 1954

Hernández-García L., Masegosa J., González-Martín O., Márquez I., Guainazzi M., Panessa F., 2017, *A&A*, 602, A65

Itoh T. et al., 2008, *PASJ*, 60, S251

Jiang J. et al., 2019, *MNRAS*, 489, 3436

Jiang J., Gallo L. C., Fabian A. C., Parker M. L., Reynolds C. S., 2020, *MNRAS*, 498, 3888

Jiménez-Bailón E., Guainazzi M., Matt G., Bianchi S., Krongold Y., Piconcelli E., Santos Lleó M., Schartel N., 2008, in Benítez E., Cruz-González I., Krongold Y., eds, *Revista Mexicana de Astronomía y Astrofísica Conference Series*, Vol. 32, The Nuclear Region, Host Galaxy and Environment of Active Galaxies. p. 131

Jin C., Done C., Ward M., Gierliński M., Mullaney J., 2009, *MNRAS*, 398, L16

Kamraj N. et al., 2019, *ApJ*, 887, 255

Kara E. et al., 2015, *MNRAS*, 446, 737

Kara E., Alston W. N., Fabian A. C., Cackett E. M., Uttley P., Reynolds C. S., Zoghbi A., 2016, *MNRAS*, 462, 511

Kaspi S., Maoz D., Netzer H., Peterson B. M., Vestergaard M., Jannuzi B. T., 2005, *ApJ*, 629, 61

Laha S., Dewangan G. C., Kembhavi A. K., 2011, *ApJ*, 734, 75

Laha S., Markowitz A. G., Krumpe M., Nikutta R., Rothschild R., Saha T., 2020, *ApJ*, 897, 66

Lansbury G. B., Banerji M., Fabian A. C., Temple M. J., 2020, *MNRAS*, 495, 2652

Laor A., Draine B. T., 1993, *ApJ*, 402, 441

Liedahl D. A., Osterheld A. L., Goldstein W. H., 1995, *ApJ*, 438, L115

Liu Y., Li X., 2015, *MNRAS*, 448, L53

Markowitz A. G., Krumpe M., Nikutta R., 2014, *MNRAS*, 439, 1403

Miller J. S., Goodrich R. W., 1990, *ApJ*, 355, 456

Murphy K. D., Yaqoob T., 2009, *MNRAS*, 397, 1549

Murray N., Quataert E., Thompson T. A., 2005, *ApJ*, 618, 569

Nenkova M., Sirocky M. M., Ivezić, Ž., Elitzur M., 2008, *ApJ*, 685, 147

Newman J., Tsuruta S., Liebmann A. C., Kunieda H., Haba Y., 2021, *ApJ*, 907, 45

Ohsuga K., Mori M., Nakamoto T., Mineshige S., 2005, *ApJ*, 628, 368

Osterbrock D. E., Pogge R. W., 1985, *ApJ*, 297, 166

Piconcelli E., Miniutti G., Ranalli P., Feruglio C., Fiore F., Maiolino R., 2013, *MNRAS*, 428, 1185

Ricci C. et al., 2017a, *ApJS*, 233, 17

Ricci C. et al., 2017b, *Nature*, 549, 488

Riffel R., Rodríguez-Ardila A., Pastoriza M. G., 2006, *A&A*, 457, 61

Risaliti G., Elvis M., Nicastro F., 2002, *ApJ*, 571, 234

Rodríguez-Ardila A., Mazzalay X., 2006, *MNRAS*, 367, L57

Rush B., Malkan M. A., Fink H. H., Voges W., 1996, *ApJ*, 471, 190

Ryan C. J., De Robertis M. M., Virani S., Laor A., Dawson P. C., 2007, *ApJ*, 654, 799

Scoville N., Norman C., 1995, *ApJ*, 451, 510

Simm T. et al., 2018, *MNRAS*, 480, 4912

Smith J. E., Young S., Robinson A., Corbett E. A., Giannuzzo M. E., Axon D. J., Hough J. H., 2002, *MNRAS*, 335, 773

Smith J. E., Robinson A., Alexander D. M., Young S., Axon D. J., Corbett E. A., 2004, *MNRAS*, 350, 140

Svoboda J., Beuchert T., Guainazzi M., Longinotti A. L., Piconcelli E., Wilms J., 2015, *A&A*, 578, A96

Ulvestad J. S., Antonucci R. R. J., Goodrich R. W., 1995, *AJ*, 109, 81

Urry C. M., Padovani P., 1995, *PASP*, 107, 803

Vasudevan R. V., Fabian A. C., 2007, *MNRAS*, 381, 1235

Véron-Cetty M. P., Véron P., Gonçalves A. C., 2001, *A&A*, 372, 730

Walton D. J., Nardini E., Fabian A. C., Gallo L. C., Reis R. C., 2013, *MNRAS*, 428, 2901

Willingale R., Starling R. L. C., Beardmore A. P., Tanvir N. R., O'Brien P. T., 2013, *MNRAS*, 431, 394

Yao S., Qiao E., Wu X.-B., You B., 2018, *MNRAS*, 477, 1356

Young S., Hough J. H., Efstathiou A., Wills B. J., Bailey J. A., Ward M. J., Axon D. J., 1996, *MNRAS*, 281, 1206

## APPENDIX A: MYTORUS MODEL

Previously, the mytorus model (Murphy & Yaqoob 2009) has been extensively used for spectral modelling of nearby obscured AGNs. In the mytorus model, the covering factor of a toroidal-shaped torus is fixed at 50 per cent of the sky (a half-opening angle of  $60^\circ$ ). This limitation causes inconsistency of the normalizations of the reprocessed spectrum, including the Compton scattering emission and line spectra, with the torus geometry. This decoupling problem is, however, required for high signal-to-noise broad-band data (e.g. Guainazzi et al. 2016).

Another limitation of the available mytorus grids<sup>2</sup> is the range of the photon index parameter. The hard upper limit of the photon index in the public version of mytorus is 2.5, which is too low for the X-ray spectra of Mrk 1239.

In this appendix, we present analysis using the mytorus model. The full model is `constant1 * tbnew * zmshift * (vmekal1 + vmekal2 + mtab(trans.abs) * cutoffpl1 + constant2 * cutoffpl2 + constant3 * atab(scattered) + constant4 * atab(fluor))` in the XSPEC format. The `tbnew` model accounts for Galactic absorption. The `zmshift` model accounts for source redshift. The `vmekal1,2` model calculates the emission from diffuse hot plasma as in MO4. The `trans.abs` model calculates photoelectric-absorbed zeroth-order continuum. The `scattered` model calculates Compton-scattering emission of the torus. The `fluor` accounts for fluorescence emissions for neutral Fe  $K\alpha$ , Fe  $K\beta$  and their Compton shoulders. The normalizations of the `cutoffpl1,2` models are linked. The coupled mode of the mytorus model is used. The `constant3` and `constant4` models, which account for the scaling factors for the scattered emission and the fluorescent line emission, respectively, are linked in our analysis.

The best-fitting parameters are shown in Table A1, and the corresponding models are shown in Fig. A1. The mytorus model provides a much worse fit to the data than MO4 – our fit shows that the data requires  $\Gamma$  to be higher than 2.5. Significant residuals are shown around 6–10 keV band as shown by the *NuSTAR* data/model ratio plot.

Despite the limited range of  $\Gamma$ , the best-fitting mytorus model suggests  $N_{\text{H,ave}} = 8_{-2}^{+4} \times 10^{24} \text{ cm}^{-2}$ , which is consistent with the value given by the `borus02` model ( $\log(N_{\text{H,ave}}) = 25.0 \pm 0.2$ ). The line-of-sight column density  $N_{\text{H,los}}$  is slightly lower than the values measured by the `borus02` model due to an improper  $\Gamma$ .

The covering factor of the torus in the mytorus model is fixed. The inclination angle of the torus is not constrained by the mytorus model. A 90 per cent confidence upper limit of  $70^\circ$  is obtained. In comparison, the upper limit of the inclination angle given by the `borus02` model is  $52^\circ$  when both  $i$  and  $C_{\text{fact}}$  parameters are free to vary (see Section 3.4.1 for more information).

<sup>2</sup>The models are available for downloads on the mytorus website at <http://mytorus.com>.

**Table A1.** Best-fitting model parameters obtained by fitting the reprocessed emission using *mytorus*. The half-opening angle of the torus is fixed at  $60^\circ$  in this model. The high energy cut-off of power-law continuum emission is fixed at 400 keV. The scaling factor for the fluorescent line emission  $A_l$  is coupled with that for the scattered continuum  $A_s$ .  $f_s$  is the scattering fraction due to optically thin matters outside the LOS.

Model	Parameter	Unit	Su	Nu&Sw
tbnew	$N_H$	$10^{20} \text{ cm}^{-2}$	$3.7 \pm 0.2$	$l$
trans.abs	$N_{H,\text{los}}$	$10^{22} \text{ cm}^{-2}$	$36 \pm 3$	$17 \pm 2$
	norm	$10^{-3}$	$3.3 \pm 0.3$	$5.5 \pm 0.6$
scattered	$N_{H,\text{ave}}$	$10^{24} \text{ cm}^{-2}$	$8^{+4}_{-2}$	$l$
	$E_{\text{cut}}$	keV	400	$l$
	$i$	deg	$<70$	$l$
	$\Gamma$	–	$>2.49$	$>2.49$
constant3	$A_s$	–	$17^{+7}_{-10}$	$15 \pm 9$
constant4	$A_l$	–	$=A_s$	$=A_s$
constant2	$f_s$	$10^{-3}$	$2.6^{+0.5}_{-0.4}$	$8.40^{+0.10}_{-0.07}$
vmekal2	kT	keV	$0.58^{+0.06}_{-0.05}$	$l$
	$Z_{\text{Ne}}$	$Z_\odot$	$4.3^{+2.2}_{-1.4}$	$l$
	norm	$10^{-5}$	$4.5^{+1.5}_{-1.2}$	$l$
vmekal1	kT	keV	$0.182^{+0.017}_{-0.016}$	$l$
	norm	$10^{-4}$	$1.6 \pm 0.3$	$l$
	$\chi^2/\nu$		562.69/469	

## APPENDIX B: CONTRIBUTION OF DISC REFLECTION IN THE X-RAY BAND

Despite the obscured X-ray emission, the power-law component from the hot corona in the AGN of Mrk 1239 is like the one in a typical high- $\lambda_{\text{Edd}}$  NLS1 (Gallo 2018): a very soft power-law index of  $\Gamma = 2.6\text{--}3.0$  is suggested by the data. Reflection off the innermost accretion disc region has been commonly seen in the X-ray observations of other unobscured NLS1s. Prominent features of disc reflection spectra include broad Fe  $K\alpha$  emission and Compton hump in the hard X-ray band. In particular, Seyfert 1 AGNs often show excess emission in the soft X-ray band, which could be part of disc reflection as well (e.g. Jiang et al. 2019). A strong supporting evidence of soft excess emission being reflection is the increasing number of discoveries of reverberation lags in the soft X-ray band (e.g. Kara et al. 2016). They are similar to the iron emission and Compton hump reverberation lags (e.g. Kara et al. 2015, 2016).

The soft X-ray emission from the centre of the AGN in Mrk 1239 is unfortunately obscured by line-of-sight column density. The iron band of Mrk 1239 is dominated by fluorescence emissions of the torus. But some disc reflection may still exist (Buhariwalla et al. 2020) and make contribution in the hard X-ray band, the observed Compton hump in particular.

In this section, we estimate the upper limit of the contribution from a disc reflection component in the X-ray band. We add the *relxill* model (García et al. 2013; Dauser et al. 2016) to MO4. The *relxill* calculates reflection spectra of a relativistic thin disc. We use a power-law emissivity profile for the disc parametrized by an index  $q$ . The inner disc inclination angle is linked to the inclination angle of the torus, although they might be different in reality. The  $E_{\text{cut}}$  and  $\Gamma$  parameters of *relxill* are linked to

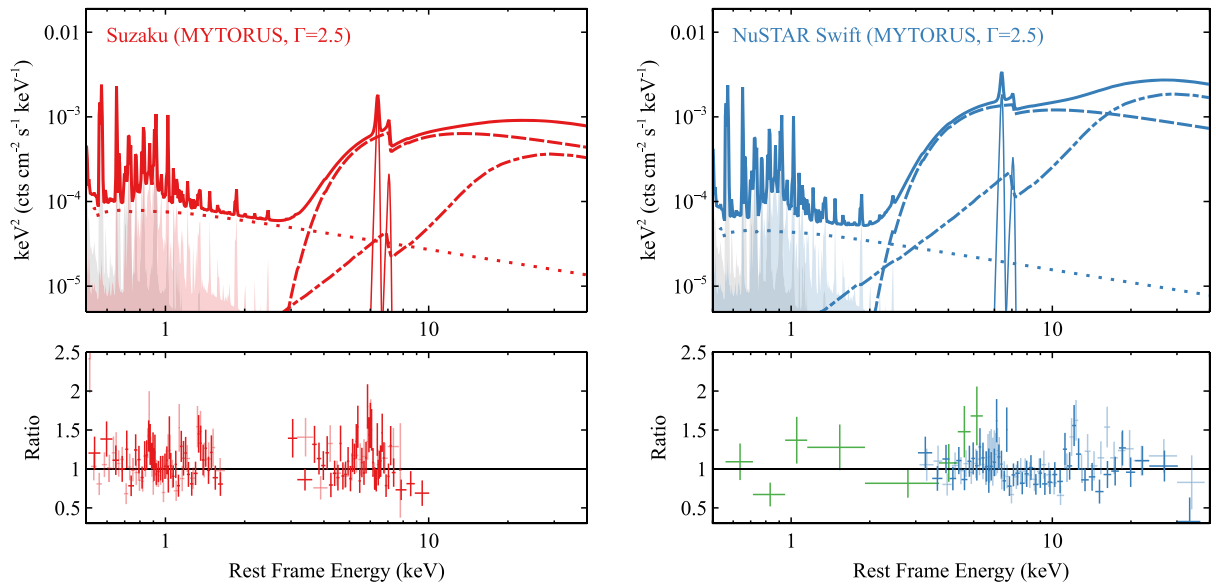


**Figure A1.** Top: best-fitting models for the *Suzaku* (left) and *NuSTAR* and *Swift* (right) spectra of Mrk 1239 using the *mytorus* model. Thick lines: total model; shaded regions: two diffuse hot plasma emission components; dash-dotted lines: Compton-scattering continuum; dashed lines: absorbed power-law continuum emission; dotted lines: scattered power-law component; thin solid lines: torus line spectra. Bottom: corresponding data/model ratio plots. Due to the limited range of  $\Gamma$  in the public *mytorus* model, the photon index is pegged at 2.5 during the analysis of both two sets of data.

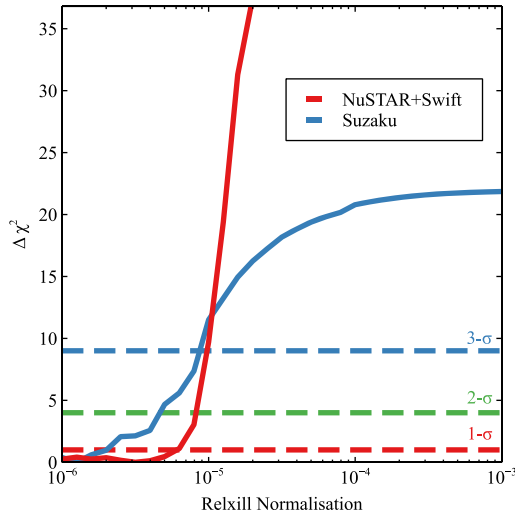


**Figure B1.**  $\chi^2$  distributions for the normalization parameter of the `relxill` model. Only upper limits are obtained. All the spectra are fitted together. The normalization parameter is allowed to be different for different epochs. The red solid line shows the measurement using the *NuSTAR* and *Swift* observations. The blue solid line shows the measurement using the *Suzaku* observation. The dashed lines show  $1\sigma$ ,  $2\sigma$ , and  $3\sigma$  uncertainty ranges.

the corresponding parameters in `borus02`. Other free parameters include the normalization parameter, the disc ionization, and the spin of the BH. The inner radius of the disc is assumed to be at the innermost stable circular orbit. By doing so, we only obtain an upper limit of the `relxill` component for both the *Suzaku* and the *NuSTAR* epochs. See Fig. B1 for the constraints of the normalization parameters of `relxill` for two epochs.

The  $3\sigma$  upper limit of the normalization parameters of `relxill` is approximately  $10^{-5}$  for both epochs. At the  $3\sigma$  upper limit, the `relxill` component produces an observed flux of approximately

$3 \times 10^{-14} \text{ erg cm}^{-2} \text{ s}^{-1}$  in the 3–10 keV band for the *Suzaku* epoch and an observed flux of around  $6.8 \times 10^{-13} \text{ erg cm}^{-2} \text{ s}^{-1}$  in the 3–78 keV band for the *NuSTAR* epoch. They, respectively, take up 4 per cent and 8 per cent of the total observed X-ray flux in corresponding total energy bands.<sup>3</sup> We conclude that the narrow Fe K $\alpha$  emission and the Compton hump shown in the X-ray observations are likely to be dominated by reprocessed emission from the torus based on the obscured X-ray nature and observations in other wavelengths (Smith et al. 2004; Rodríguez-Ardila & Mazzalay 2006). The inner disc reflection makes little contribution to the data with a  $3\sigma$  upper limit of 8 per cent during the *NuSTAR* epoch.

The lack of evidence for broad Fe K $\alpha$  emission is interesting. Following are possible explanations: (1) the disc might be very ionized. As shown by Jiang et al. (2020), the discs in some very extreme, unobscured NLS1s with  $\Gamma > 2.5$  show a high ionization state of  $\log(\xi) > 3$ . In comparison, typical Seyfert AGNs have a lower-ionization disc of  $\log(\xi) \approx 1\text{--}2$  (Walton et al. 2013). At such a high ionization state, the Fe K $\alpha$  emission is weak (e.g. García et al. 2013). (2) The high- $\lambda_{\text{Edd}}$  NLS1s in Jiang et al. (2020) and Mrk 1239 are all very soft X-ray emitters. The S/N of the current X-ray CCD data, e.g. from *XMM-Newton* or *Suzaku*, is not high enough to detect their broad Fe K $\alpha$  emission. Future high-S/N observations, e.g. from *Athena*, might be able to do so according to the simulations in Jiang et al. (2020). (3) The innermost accretion region may not hold a thin disc geometry at a high Eddington ratio as in Mrk 1239. Due to the thickness of an optically thick disc, emissions from the innermost region might be obscured by the puffed-up disc (e.g. Ohsuga et al. 2005). Consequently, a lower reflection fraction is expected for an optically thick, geometrically slim disc with a compact coronal region in comparison with a geometrically thin disc.

<sup>3</sup>The `relxill` component takes up to 6 per cent and 9 per cent in the 10–40 keV band, respectively, for the *NuSTAR* and *Suzaku* epochs.